Article:
Liu, G., Zhao, M., Liu, K. et al. (3 more authors) (2023) Comparative study of performance of wicking and conventional railway geotextiles under the synergetic simulation of train loads and flooding. Construction and Building Materials, 400. 132840. ISSN 0950-0618

https://doi.org/10.1016/j.conbuildmat.2023.132840

Comparative experimental study of wicking and conventional geotextiles affecting ballast–subgrade performance under the synergetic effects of train loads and flooding simulation

Gang Liu[1], Mingzhi Zhao[2], Kaiwen Liu[3*], David P. Connolly[4], Xin Jiang[5], Lei Zhang[6]

[1]Associate Professor, School of Architecture and Civil Engineering, Xihua University, Chengdu 610039, Sichuan, China.
E-Mail: 0120130047@mail.xhu.edu.cn

[2]Associate Professor, School of Architecture and Civil Engineering, Xihua University, Chengdu 610039, Sichuan, China.
E-mail: 1220180013@mail.xhu.edu.cn

[3]Associate professor, MOE Key Laboratory of High-speed Railway Engineering, Southwest Jiaotong University, Chengdu, 610031, Sichuan, China (*corresponding author).
E-mail: kaiwen.liu@queensu.ca

[4]Institute for High Speed Rail and Systems Integration, School of Civil Engineering, University of Leeds, UK.
E-mail: d.connolly@leeds.ac.uk

[5]Professor, MOE Key Laboratory of High-speed Railway Engineering, Southwest Jiaotong University, Chengdu, 610031, Sichuan, China.
E-mail: xjiang01@home.swjtu.edu.cn

[6]Ph. D Candidate, MOE Key Laboratory of High-speed Railway Engineering, Southwest Jiaotong University, Chengdu, 610031, Sichuan, China.
E-mail: zhanglei30270429@163.com

Comparative experimental study of wicking and conventional geotextiles affecting ballast–subgrade performance under the synergetic effects of train loads and flooding simulation

Abstract: Geotextiles are used within railways and highways to reduce settlement and improve drainage characteristics. However the drainage performance of conventional geotextiles under unsaturated conditions can be limited due to capillary barrier effects. Therefore more recently, wicking geotextiles consisting of woven fibers with deep groves have been developed to improve drainage performance. Despite these potential performance benefits, although there have been numerous highway studies, there has been minimal study into the performance of wicking geotextiles for railways. Therefore this study performs large-scale laboratory tests on railway ballast-subgrade materials under three conditions: non-stabilized (NSS), conventional geotextile stabilized (CGSS), and wicking geotextile stabilized (WGSS). Each test sample is subject to 600,000 cyclic loading cycles over 3 phases. The first phase a stationary phase for consolidation, the second is to simulate loading directly after rainfall, and the third is to simulate loading after flooding. The results are analyzed and four conclusions are drawn: 1) both geotextile types prevent rainfall water from infiltrating into subgrade soils, however the wicking shows elevated performance, 2) the wicking geotextile produces capillary suction, which compared to the conventional geotextile, significantly delays infiltration and helps to reduce the moisture content in subgrade soils, 3) both geotextiles are capable of separation and filtration during rainfall and flooding simulation, however the wicking offers additional performance, 4) the deformation of both geotextiles is similar.

Key words: Wicking geotextile; railway engineering; moisture content; ballast fouling; ballast–subgrade performance; surface settlement

1 Introduction

The serviceability of earth structures can be improved using reinforcement agents and geosynthetics [1,2]. Among other methods, geotextiles are commonly adopted for separation, filtration, reinforcement, stabilization [4-8], protection and drainage [3]. The functions of geotextiles can be divided into mechanical and hydraulic applications when laid at the interface of subgrade and sub-ballast/sub-base [9,10]. Regarding mechanical behavior, woven geotextiles provide lateral restraint for the overlying structural layer, increase the strength and stiffness of the sub-ballast or sub-base layer, stabilize the soil–geotextile system, reduce the vertical stress over the subgrade and decrease the settlement of the embankment [11].

Regarding hydraulic behaviour, woven geotextiles serve as filters to minimise the softening of subgrade layers, prevent fine particles from migrating upwards and maintaining the ballasted layers in a clean condition. The opening size of a geotextile needs to be carefully designed in order to obtain a sufficient filtration capacity [12]. Regardless of design though, conventional woven geotextiles are difficult to use as an effective drainage passage under unsaturated conditions due to the presence of hydrophobic materials, typically resulting from the initial unsaturated state of the geotextile [13-16]. Therefore, despite the potential mechanical benefits, the hydraulic benefits are impeded by this capillary barrier effect.

In recent years, wicking geotextiles, a new type of geotextile, have been developed. Deep-grooved wicking fibers are embedded into the geotextiles to wick water from the unsaturated material. The wicking fibers produce a large quantity of microchannels that can generate capillary suction, similar to the small pores in unsaturated soils. The suction difference between geotextiles and unsaturated soils forms a driven force that compels pore water in soil voids to migrate toward the geotextile [17,18]. The water at the exposed portion of the geotextile evaporates into the air, generating a suction difference between the exposed portion and the portion buried at the interface. Therefore, a suction gradient forms in unsaturated soils, spanning the buried portion of the geotextile to the exposed portion, leading to smooth water drainage in the wicking geotextile [19,20]. Lin and Zhang [15] obtained the geotextile–water characteristic curves (GWCC) of conventional and wicking geotextiles by performing a capillary rise test, a pressure plate test, and a salt concentration test. The GWCCs showed that the conventional geotextiles could not hold water under unsaturated

conditions, but the wicking geotextiles can hold and transport water smoothly. Further, Bai et al. [21] conducted a rainfall simulation test on a kaolinite soil column, finding that the wicking geotextile could produce sufficient capillary force to drain both the gravitational and capillary water out of the kaolinite soil.

The effectiveness of wicking geotextiles for soil moisture reduction and service performance improvement for roadways has been discussed in previous literature. For example, a series of laboratory tests were conducted to study the working mechanism of soil–wicking geotextile systems [22]. It was shown that the wicking fabric served as an effective drainage material to prevent capillary water from rising upward to the base course of the roadway. Wang et al. [17] also performed a physical model test to evaluate the effectiveness of wicking geotextiles for roadway applications. They concluded that wicking geotextiles can effectively wick water out of road sections compacted close to optimum water content, and the moisture content of the base course after rainfall remains close to that before rainfall due to the water drainage function of the geotextile. Further, [23] used full-scale model testing to show the wicking geotextile was able to drain overlying soils, with water content of initially saturated soil decreasing from 12.5% to 8.9% within 1 h. Guo et al. [10] conducted a comparative study to illustrate the effects of wicking geotextiles on the service performance of a roadway embankment. The results showed the wicking fibers in the geotextile provided effective drainage for the infiltrated water during and after rainfall and further reduced the permanent deformation of the road section. Lin et al. [24] reported the application of wicking geotextiles on Dalton Highway to alleviate a frost boil issue. The initial 2 years of operation showed the wicking geotextile was able to mitigate frost heave and the subsequent thaw weakening issues. Moreover, wicking geotextiles were incorporated into 500-ft-long test sections of State Highway 21 in Texas. The monitoring results showed the highway section stabilized using wicking geotextile maintained a uniform water content for the soil in contact with the geosynthetic. The geotextile also helped to prevent cracking of the pavement above [25].

Although the effectiveness of wicking geotextiles for highways has been studied in the literature, the hydraulic and mechanical stabilization performance for railways has received limited attention. This is particularly true considering train loading conditions and flooding. Therefore in this paper, a series of large-scale physical model tests are performed on NSS, CGSS and WGSS to

compare the effects of wicking and conventional geotextiles on the service performance of railway embankments. A series of cyclic loading sequences are applied after stationary, rainfall, and flooding simulations. The effect of WGSS on the service performance of ballast–subgrade is investigated by measuring moisture content variation, ballast fouling and permanent deformation.

2 Material properties

The test model was constructed with three distinct layers: (1) a lower silty clay subgrade layer with a thickness of 0.7 m, overlain by (2) a 0.15-m-thick sub-ballast layer, overlain by (3) a 0.3-m-thick ballast layer. The subgrade layer was a silty clay with an average grain size D_{50} of 0.015 mm. Fig. 1 shows the gradation curve of the subgrade material. The uniformity coefficient of the subgrade material was 11.1, and the gradation coefficient was 1.0. The liquid and plastic limits were 36.0% and 22.9%, respectively, obtained using the liquid–plastic limit method. Fig. 2 presents the compaction curve of the subgrade material obtained using the modified Proctor method. The maximum dry density of the material was 1.65 g/cm^3, and the optimum moisture content was 18.3%. The permeability of the subgrade was 6.12×10^{-8} m/s, evaluated using a falling head permeameter at degree of compaction of 0.9 based on the maximum dry density.

To investigate the effect of moisture content on the strength properties of the subgrade materials, CBR (California Bearing Capacity) tests were performed for the silty clay with different water contents. Since the saturated moisture content of the silty clay at a degree of compaction of 0.9 was measured to be 30.7%, the target moisture contents were: 18.3%, 22.4%, 26.5% and 30.7%, respectively. The silty clays were constructed in 5 layers in a rigid mould to produce a soil column with degree of compaction of 0.9. The variation of CBR of the silty clay against moisture content is presented in Fig. 3. As moisture content of the silty clay increases from 18.5% to 26.1%, CBR decreases sharply from 27.0% to 1.4%. This highlights the advantage of controlling the moisture content in this range for in-service railway subgrades.

The sub-ballast and ballast were basalt and granite, respectively, sourced from Sichuan Province, China. The grain size distributions of the sub-ballast and ballast are also presented in Fig. 1. The average grain size D_{50} of the sub-ballast layer was 8.37 mm. The uniformity and gradation coefficients of the sub-ballast layer were 14.06 and 1.35, respectively. The gradation of the ballast

layer was designed according to the railway industry standard of PRC: Railway ballast (TB/T 2140-2008). The average grain size D_{50} of the ballast layer was 38.51 mm.

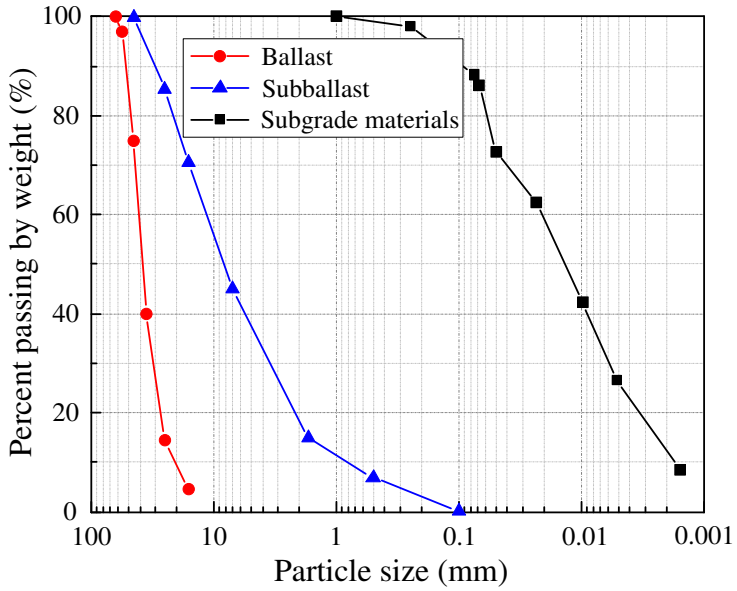

Fig. 1 Grain size distribution of ballast, sub-ballast and subgrade materials

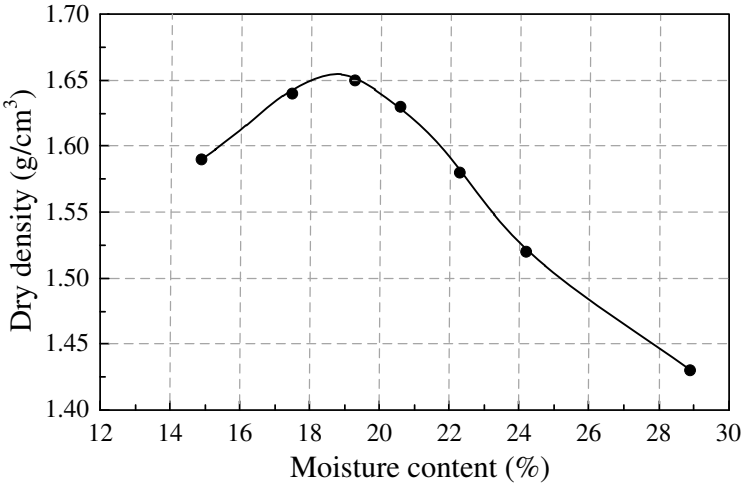

Fig. 2 Compaction curves of the subgrade materials based on the modified Proctor method

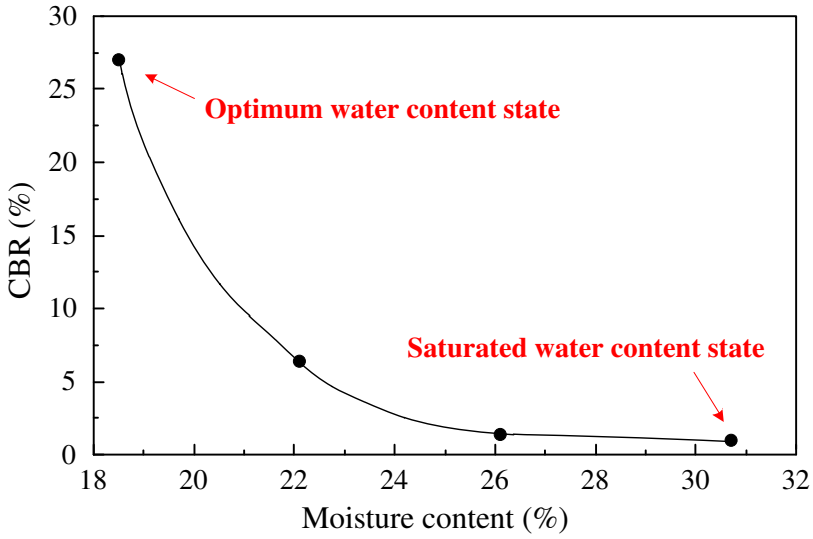

Fig. 3 The variation of CBR against moisture content for the subgrade materials

A conventional woven geotextile with similar mechanical properties to the wicking one was used to compare the suction and drainage effects considering a railway section. Fig. 4 shows the both geotextiles. Table 1 presents the comparison of the physical properties of these geotextiles. The opening size of the wicking geotextile was 0.12 mm, which was close to that of the conventional geotextile (0.14 mm). The cross-plane permeability of the wicking geotextile was measured using the constant head method and found to be 0.21 cm/s, which is slightly lower than that of the conventional geotextile. However, the in-plane flow rate of the wicking geotextile was almost double that of the conventional geotextile in both machine and cross-machine directions.

Table 1 Properties of geotextiles (provided by the manufacturer)

Properties	Test standard	Unit	Minimum Average Roll Value	
			Conventional geotextile	Wicking geotextile
CBR puncture strength	ISO 12236	kN	12.4	14
Drop cone diameter	ISO 13433	mm	3.1	3.0
Opening size	ISO 12956	mm	0.14	0.12
Cross-plane permeability	ISO 11058	cm/s	0.25	0.21
MD in-plane flow rate	ISO 12948	liters/m/h	39.2	74.3
CD in-plane flow rate	ISO 12948	liters/m/h	40	87.7

Note: MD=machine direction and CD=cross-machine direction.

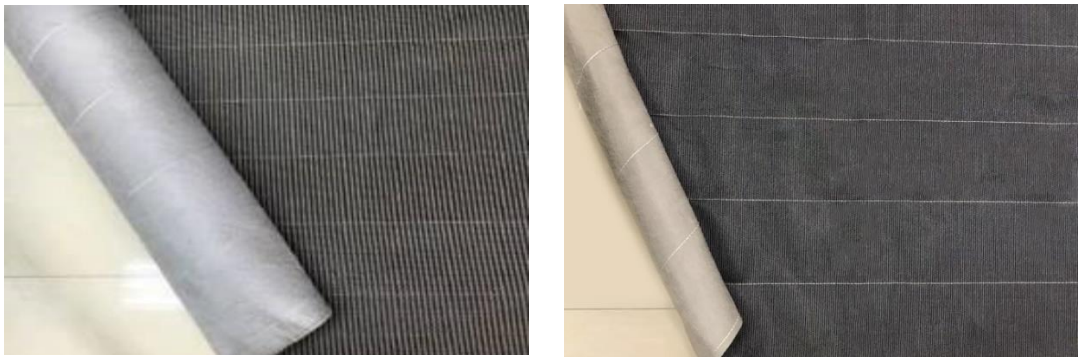

(a) Conventional geotextile (b) Wicking geotextile

Fig. 4 The geotextiles adopted in this study

3 Test setup and procedure

3.1 Test setup

Three test sections (i.e. NSS, CGSS and WGSS), were constructed to evaluate the influence on the ballast–subgrade performance. Several parameters were monitored during the test to perform a comparative study between the wicking and conventional geotextiles. The moisture content in the subgrade was recorded at different depths to evaluate the effect of wicking drainage. The pore water pressure below the ballast–subgrade interface was also carefully monitored during the testing process to illustrate the fouling degree of the ballast layers. Finally, the settlements at ballast surface, top ballast and sub-ballast interface (TS interface), sub-ballast and subgrade interface (SS interface) were measured for the three test sections.

The loading plate was designed to simulate the contact stress distribution at the ballast–tie interface. Fig. 5 illustrates the typical contact stress distribution at the interface for a standard gauge track based on the relationship proposed by Mchenry et al. [26] and Atalar et al. [27]. The stress distribution area had a length of 1100 mm under each rail in the transverse direction, and the width of the stress distribution area was 300 mm in the longitudinal direction in terms of the bottom width of the tie. Therefore, the plan view scale of the loading plate is 1100 mm in length and 300 mm in width, thus simulating the stress distribution at the ballast–tie interface. Given the cyclic loading amplitude, the thickness of the loading plate was 25 mm to prevent bending. To avoid stress concentration at some individual points and ensure even load transmission, a sandbag with dimensions of 1.4 m × 0.6 m × 0.02 m was placed between the loading plate and the ballast bed. The sandbag material was a coarse sand with a diameter of 1–2 mm.

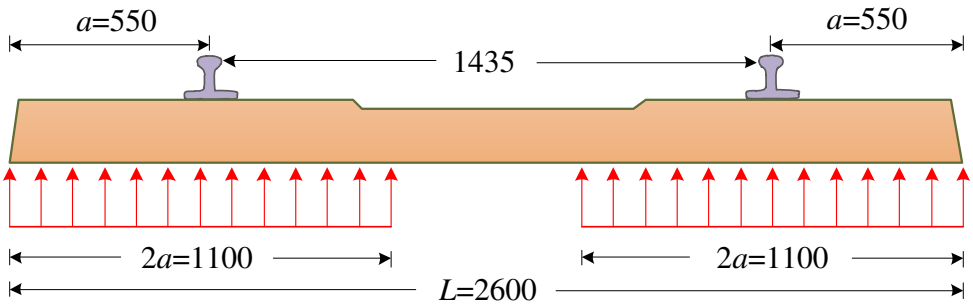

Fig. 5 Stress distribution in the transverse direction (unit: mm)

The dimensions of the model box were determined based on the area of influence in the plane and interacted depth of the stress applied by the loading plate. An elastic finite element model measuring 5.5 m in length, 1.5 m in width, and 3.0 m in height was established to evaluate the range of influence of the stress. A uniformly distributed load with an area of 1.1 m × 0.3 m was applied at the center of the model. The load intensity was 48 kN and is discussed in detail hereinafter. The results showed the horizontal stress was attenuated by nearly 80% at 0.15 m away from the edge of the uniformly distributed load in the length and width directions. Additionally, the vertical stress decreased by more than 90% at 1.2 m depth. Therefore, the filling model was designed with dimensions of 1.4 m in length, 0.6 m in width, and 1.2 m in height.

A rigid model box with a clearance of 1.5 m in length, 0.7 m in width, and 1.3 m in height was fabricated with 0.5-cm-thick steel plates in consideration of foam layer and connecting hole at the bottom (Fig. 6). To assess the potential for boundary effects impacting testing precision, finite element analysis was performed and a polystyrene foam layer with thickness of 5 cm was concluded to be sufficient to minimize reflections. Therefore this was constructed in the box. A gravel layer with a thickness of 0.1 m was laid at the bottom of the box to facilitate water drainage for the rainfall simulations and to form communicating vessels to monitor water level in the flooding simulations, as shown in Fig. 6(a). Drainage and connecting holes with a diameter 3 cm were drilled through the steel plate and polystyrene foam layer along the length of the model box, which was directed at the bottom gravel layer for water drainage and water level monitoring. Three holes were distributed on each side, as shown in Fig. 6(b). The subgrade section was constructed above the gravel in five layers using silty clay at optimum water content. The lower four layers were compacted in 150 mm lifts, and the top layer was constructed in a 100 mm lift. The degree of compaction was controlled at 0.9 based on the maximum dry density of the silty clay. The sub-ballast section was filled to reach

a density of 2.00 g/cm^3. The ballast section had a total thickness of 300 mm and was compacted in 150 mm lifts. The targeted density of the ballast layer was 1.70 g/cm^3, which complied with the railway industry standard of PRC: Railway ballast (TB/T 2140-2008). Assurance measurements for subgrade, sub-ballast, and ballast during and after the construction of each test section were taken to make reasonable comparisons of three sections.

The wicking or conventional geotextile was placed at the SS interface to investigate the effect on the service performance of the ballast–subgrade structure. The geotextile had dimensions of 2.3 m × 1.5 m (machine direction × cross-machine direction). A 0.45-m-wide edge of the geotextile was taped against the polystyrene foam in three directions to restrict its possible movement and simulate the restriction of the surrounding ballast imposed on the geotextile in the field. An excess length of 0.45 m of the geotextile was retained in the remaining short-side direction and went through the drainage seam on the steel plate and polystyrene foam layer. The drainage seam had a width of 60 cm and a height of 1 cm. The purpose of the excessive part of the geotextile that went through the drainage seam was to allow water drainage via the wicking geotextile after rainfall and flooding simulations. The drainage seam had the same elevation as the geotextile. Fig. 7 presents the photograph of the test model.

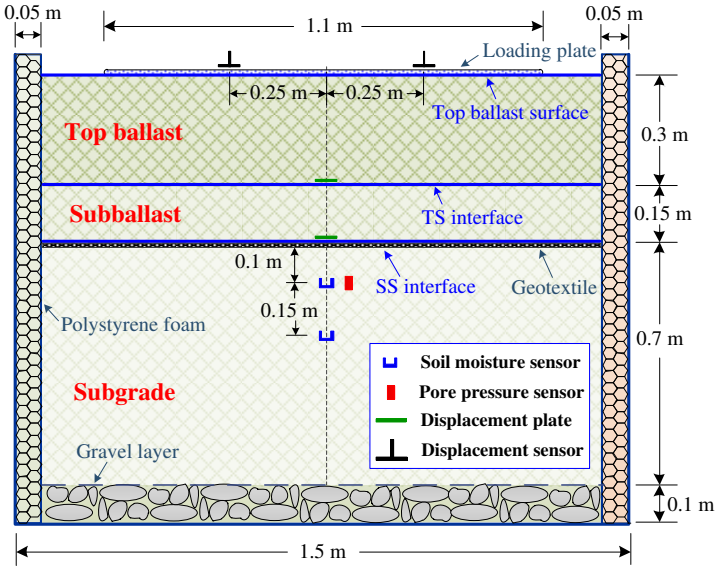

(a) Front view

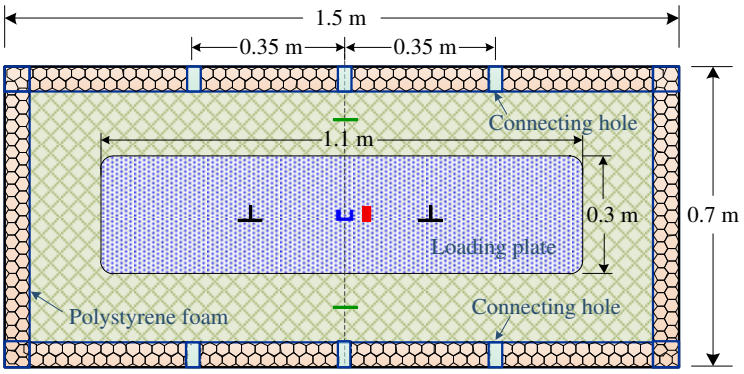

(b) Top view

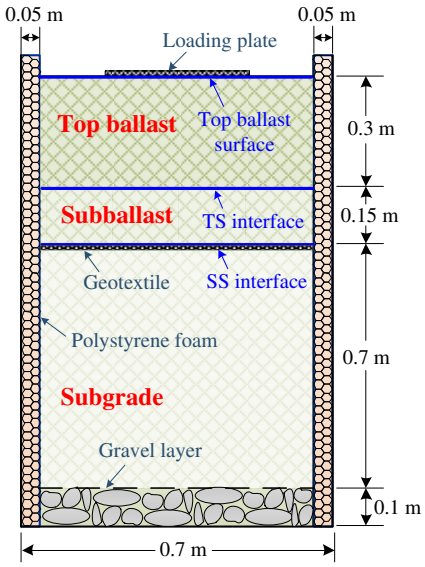

(c) Side view

Fig. 6 Test model and instrumentation: (a) front view, (b) top view and (c) side view

Fig. 7 The photograph of the test model (with rainfall simulator uninstalled)

The moisture content was monitored using a HOBO sensor probe (S-SMD-M005). The sensor probe

was 160 mm in length, 32 mm in width and 2 mm in thickness. It had a measuring range of 0-57% of volumetric moisture content. The measurement accuracy was ±3.3%. The volumetric moisture content measured by HOBO needed to be divided by the dry density of the subgrade soil to obtain the mass moisture content. Two soil moisture sensors were buried along the central line for a given test model to monitor the moisture content during rainfall and flooding simulation periods. The moisture sensors were placed at 10 and 25 cm below the SS interface, respectively. The pore pressure sensor was manufactured by Sanda Instruments Co. Ltd. The sensor was a strain gauge 19 mm in diameter and 30 mm in height. It measured pore pressure ranging from 0 to 100 kPa with a precision of ±1 με. The pore pressure sensor was placed 10 cm below the SS interface, along the central line of the test model to monitor the accumulation of pore pressure during cyclic loading. The settlements at the ballast top surface, TS interface, and SS interface of the test model were recorded by eddy current displacement sensors. The displacement sensors have a measuring range of 0~5 mm and a precision of ± 0.5 mm. The settlements at TS and SS interfaces were transmitted above the test model surface using a rigid steel tube, with a plate at the interface installed on one side of the tube and a displacement sensor attached to the other side. All sensors were calibrated before tests.

After construction of the test model, the cyclic amplitude of the load applied on the loading plate was determined reasonably to simulate the train load. Fig. 8 presents the allocation proportion of a single axle load in the longitudinal direction, as evaluated by the simplified analysis model described in [28]. As the axle load was located fitly above a single tie, it showed an effective scope of influence in longitudinal direction. Such an effective scope was determined by the rigidity of rail, tie, and ballast and evaluated to be approximately 4.71 times the elastic deflection length of the rail. The deflection length of the rail was 0.87 m under common rigid circumstances, leading to an effective influence scope of approximately 4.0 m in the longitudinal direction, which covered seven ties. However, the ties farthest away from the axle load received a negligible magnitude of stress, so the model was simplified to assume that the axle load was shared by only five ties. The allocation proportion decreased from 40% to 10% for the ties located from the middle to the sides (Fig. 8).

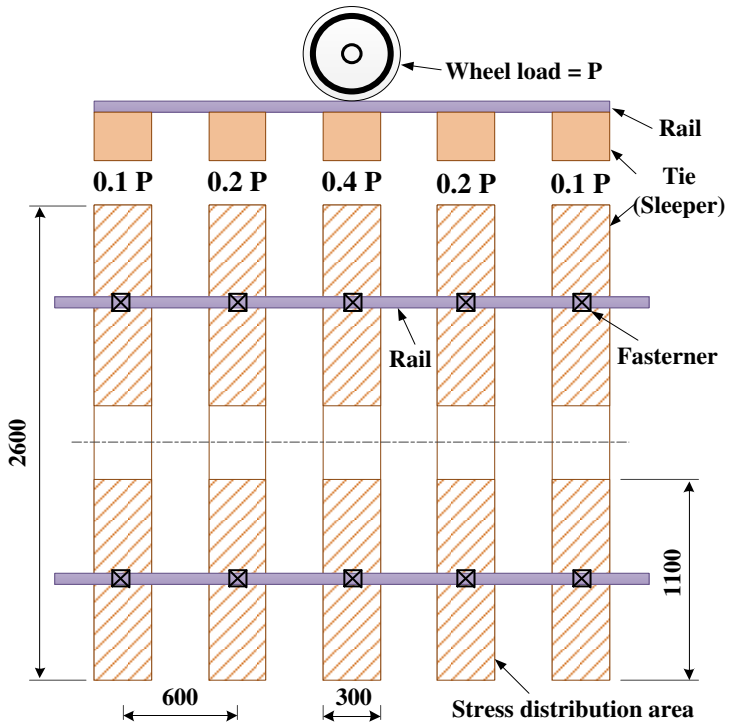

Fig. 8 Allocation proportion of a single axle load and the corresponding stress distribution area.

A typical train axial load *P* is 20 tons (≈200 kN) implying a single tie is expected to experience a maximum stress of 80 kN (=0.4 *P*). Therefore stress was applied to two identical stress distribution areas for a single tie, each with a vertical stress of 40 kN. The dynamic amplification factor was proposed to be 1.2 given the effect of operational speed of a train. Therefore the cyclic amplitude of the axle load applied on one-side of a single tie was 48 kN.

Cyclic load was applied using a multi-channel servo loading system. In the cyclic loading process, two types of loading were applied on the loading plate. One was the cyclic component for the train load simulation, and the other was the monotonic load composed of both the dead load of loading plate and 10% of the cyclic load. Initially, the dead load of loading plate, whose value was 1.06 kN, was applied to consolidate the test model. To ensure that the loading system and loading plate remained in contact during the entire loading process, a monotonic stress with a magnitude of 4.8 kN (10% of the cyclic load) was applied to the model through the loading plate. Then, a low magnitude of cyclic stress, of amplitude 8 kN, was imposed on the test section for 100 cycles at a loading frequency of 0.2 Hz in the pre-loading stage. Afterwards, the cyclic amplitude was increased to 24 kN to obtain a double amplitude (48 kN) to simulate the single axle load acting on the central tie. The loading frequency was held at 0.2 Hz for another 200 loading cycles initially. In subsequent loading cycles, the loading frequency gradually increased to 0.5 Hz for 100 loading cycles, 1 Hz for

200 loading cycles, 2 Hz for 400 loading cycles, and finally to 3 Hz for 199,000 loading cycles. Despite the increased loading frequency, the cyclic amplitude was constant at 24 kN. The loading sequence is demonstrated in Fig. 9. The 3 Hz loading frequency was selected following the work of Takemiya H [29].

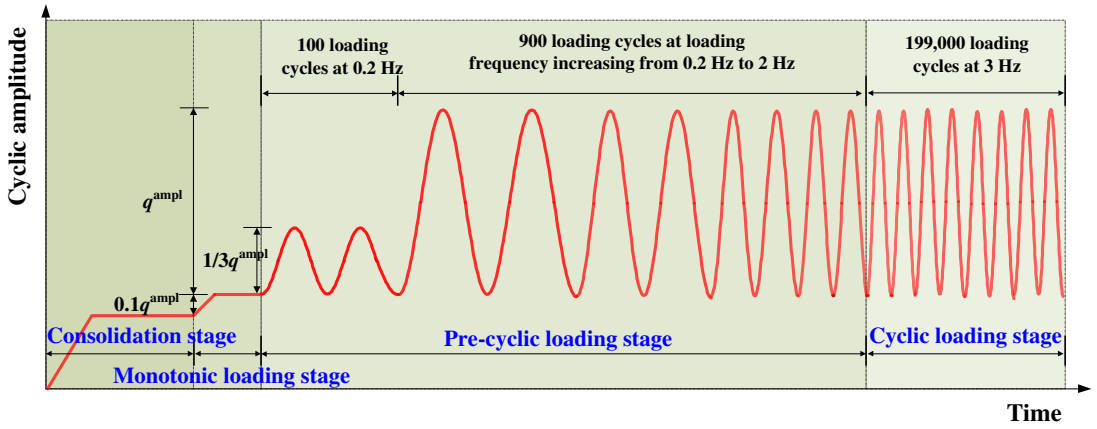

Fig. 9 Loading sequence

3.2 Test procedure

Each of the three test sections (NSS, CGSS and WGSS), was subjected to three test phases. The first phase (Phase I) was termed the 'stationary–loading' phase. The test model experienced a stationary period of 12 h upon completion of construction. After stationary simulation, it underwent cyclic loading for 200,000 cycles. The loading was imposed according to the loading sequence depicted in Fig. 9. Most of the loading cycles were applied at a loading frequency of 3 Hz. Approximately 19 h were needed for 200,000 cycles.

Then, the test model entered into Phase II, which was defined as the 'rainfall–loading' process. The rainfall simulator was installed above the test model by tying it to a steel frame once Phase I was finished. The major component of the simulator was a rainfall simulation pipeline made of polyvinyl chloride (PVC) pipes with an outer diameter of 16 mm. The rainfall simulation pipeline was composed of eight parallel PVC pipes with a length of 1520 mm and a spacing of 75 mm, resulting in an overall dimension of 1.52 m in length and 0.54 m in width for the pipeline. The two ends of the parallel pipes were connected to two PVC pipes with the same diameter using T-shape adaptors. A series of 1-mm-diameter holes with a spacing of 75 mm were drilled onto the parallel PVC pipes. A water inlet with a diameter of 25 mm was set on the midspan of the PVC pipelines,

with a glass rotameter fitted to monitor the water input during the rainfall simulation. On the other end of the water inlet pipe was a water pump that pumped water from a water tank (Fig. 10).

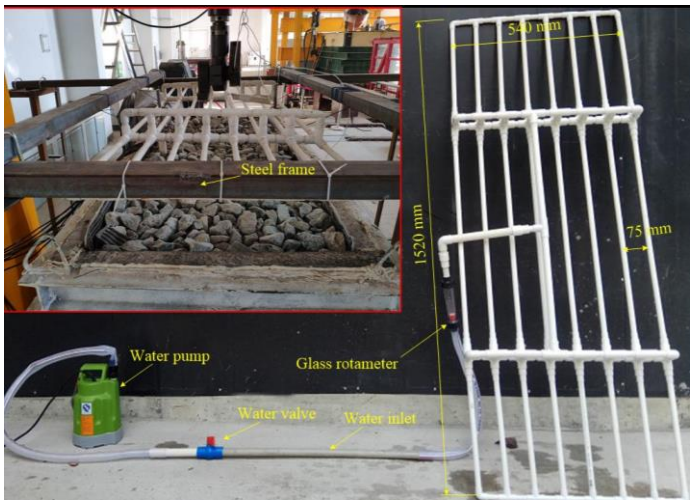

Fig. 10 The rainfall simulator

The rainfall simulation was composed of six test cycles. Each cycle included a 1 h rainfall period and a 1 h drainage period. Approximately 57 L of water was distributed to the test model in each cycle for 1 h, and the model was then left standing still for another 1 h for water drainage. Thereby, approximately 342 L of water was distributed to the test model via the rainfall simulator in 12 h. During the rainfall period, the intensity of the simulated rainfall was controlled at 67.88 mm/h with a covered area of 1.4 m × 0.6 m. The simulated rain intensity corresponded to the precipitation rate in Chengdu, Sichuan Province, where the tests were performed. The corresponding controlled water flow was 0.95 L/min. During the rainfall and drainage periods, rainfall could drain through the connecting holes at the bottom. Given the permeability of the subgrade (6.12×10^{-8} m/s), the water could not flow through the subgrade completely for a limited duration. Consequently, part of the rainfall could flow through the gap between the subgrade and foam layer. At 12 h after the rainfall simulation, 200,000 loading cycles were applied to the test model at a loading frequency of 3 Hz.

As Phase II was accomplished, the flooding–loading process was activated (Phase III). The flooding simulation was conducted by pouring water on the top of the test model. In this phase, the connecting holes at the bottom were connected to a water tank through hoses to form communicating vessels. The drainage seam was sealed using silicone adhesive to prevent water flowing out during the flooding period. The water level in the water tank was kept at the same height as the SS interface

to ensure water infiltration. A large volume of water flowed through the gap between the subgrade and foam layer initially and the water level rose to the target height within a short time. Nevertheless, as the water in the model box infiltrated into the subgrade gradually, the water level in the tank descended slowly. Therefore, some additional water was needed to replenish the water level. As the water at the bottom gravel layer transported upward into the subgrade soil, the moisture content increase in the subgrade was attributed to the water transportation from the top and bottom of the subgrade. The test section was flooded for 10 days. After 10 days of flooding, the hoses were removed from the connecting holes to permit water drainage from the test model. The drainage period lasted for approximately 12 h. Then, cyclic loading was applied for 200,000 loading cycles, and the loading sequence was in accordance with Fig. 9. The soil moisture content, pore water pressure, and settlements were monitored in real time during the abovementioned three phases. Fig. 11 demonstrates the overall test process.

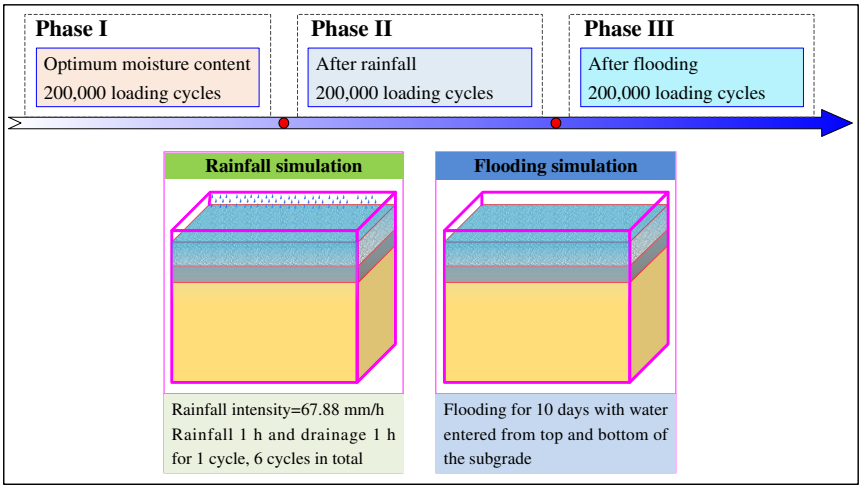

Fig. 11 Test phases

4 Test results and discussions

4.1 Moisture content variation

The subgrade sections of the three test models (NSS, CGSS and WGSS) were constructed at the optimum water content to obtain a favorable service performance. Therefore, the target moisture content of the subgrade sections was 18.6%. At the beginning of the first cyclic loading period, the soil moisture content at different depths of subgrade sections was recorded using moisture sensors (Table 2). The moisture contents at different elevations remained close to each other for a given model, indicating water was distributed uniformly along the depth for all of the test sections. The

average soil moisture content was 18.0%, 18.0%, and 17.8% for NSS, CGSS and WGSS, respectively. More importantly, the subgrade moisture content of the three test models remained stable during the first loading period. This finding implied all of the investigated test sections were in ideal conditions in Phase I.

Table 2 Moisture contents at the beginning of the first loading period

Location	NSS	CGSS	WGSS
10 cm below the interface	17.0%	18.2%	17.4%
25 cm below the interface	18.9%	17.7%	18.1%
Average value	18.0%	18.0%	17.8%

However, after a 12 h rainfall simulation period, the moisture content of subgrade at different depths increased for the tested models (Fig. 12). Fig. 12(a) shows the increase of moisture content at 10 cm below the SS interface initiated 1 h after the beginning of rainfall simulation for NSS. After 12 h of rainfall simulation, the moisture content increase remained steady at 8.5%–8.7%. By contrast, no significant moisture content increase was observed at 10 cm below the interface up to 4 h from the beginning of rainfall simulation for CGSS and WGSS. After 4 and 5 h of incubation periods, the moisture contents of WGSS and CGSS began to increase. Finally, the moisture content increase stabilized at 6.1%–6.4% for CGSS and 5.8%–6.0% for WGSS. The comparison implied both the conventional and wicking geotextiles could help to decrease the moisture content at subgrade when laid at the interface of the subgrade and sub-ballast, and the effect of reducing moisture remained similar for the two kinds of geotextiles.

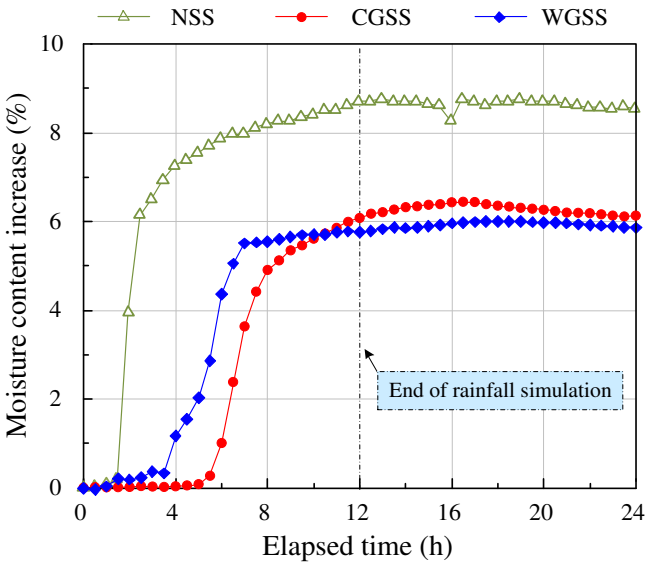

(a) 10 cm below the interface

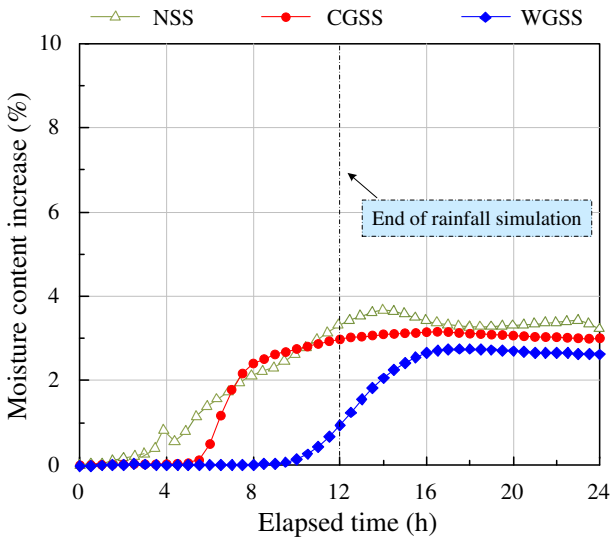

(b) 25 cm below the interface

Fig. 12 Subgrade moisture content variation during the rainfall simulation process

The moisture contents at 25 cm below the SS interface presented different features for the three test sections during and after rainfall [Fig. 12(b)]. For NSS, the moisture content at 25 cm depth of the subgrade began to increase at 3 h after the beginning of the rainfall. The increase in moisture content reached 3.53% at the end of rainfall simulation, and it fluctuated between 3.0% and 3.7% in the 12 h monitoring period afterward. However, the moisture content started to increase at 6 h and 10 h after the beginning of rainfall simulation for CGSS and WGSS respectively. This was significantly later than that of NSS.

With the relationship in Fig. 12(a) taken into consideration, it took 1 h for water transport from the SS interface to the location 10 cm below for NSS. Further, from the location 10 cm below the interface to that 25 cm below, another 2 h was needed for the water transport. For CGSS, 5 h and 1 h were spent for the above-mentioned distances of water transport respectively. In contrast, it took 4 h and 6 h for the rainfall water to finish the distances for WGSS. As rainfall water reached to the point 10 cm below the SS interface, it infiltrated downwards naturally without any influence of capillary suction from the NSS and CGSS. However, it needed significantly longer time for the water migrating from 10 cm to 25 cm below the SS interface of WGSS. This was attributed to the effect of capillary suction produced by the wicking geotextile [10,17].

The large number of micro-channels in the WGSS led to the suction difference between subgrade soil and geotextile. Therefore the rainfall water was driven to the geotextile and flew towards the

exposed portion [17,18]. Therefore, the increase in moisture content at 25 cm below the SS interface was observed much later in WGSS compared to CGSS and NSS. The moisture content increase of WGSS became steady at 2.6%–2.7%, which was notably less than the steady moisture content increase of CGSS (3.0%–3.2%) and NSS (3.0%–3.7%). The lower steady moisture contents observed at 10 and 25 cm below the interface for WGSS compared with that in CGSS may also have been due to the drainage capacity of the wicking geotextile.

Fig. 13 presents the moisture content increases in the subgrades of the tested models after flooding. The moisture content increase in the subgrade during flooding was induced not only by water infiltration from the top of the subgrade but also by the water from the bottom gravel layer. Despite this condition, the moisture content increase at 10 cm below the SS interface was 4.92% and 5.42% for WGSS and CGSS, respectively, both of which were lower than that of NSS. Similarly, at 25 cm below the SS interface, the moisture content increase of WGSS was 5.94%, which also remained the lowest among the three test sections. In contrast, NSS had the maximum moisture content increase of 7.96%. This implied both conventional and wicking geotextiles played a crucial role in restricting water from infiltrating into the subgrade. The lower moisture content increase in WGSS compared with that in CGSS was attributed to the wicking drainage capacity of the wicking fiber in WGSS.

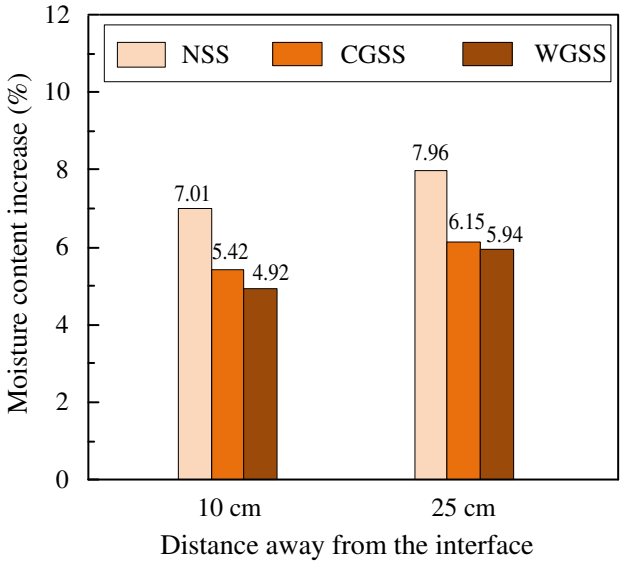

Fig. 13 Subgrade moisture content increase during the flooding simulation process

As shown in Fig. 3, the CBR of the subgrade materials decreased sharply as moisture content

went beyond the optimum value (18.3%). This implied that the in-service performance of the subgrade materials would deteriorate with increasing moisture content. Therefore, it was crucial to prevent moisture content exceeding this range. The moisture content increases in CGSS and WGSS were significantly lower than that in NSS after rainfall and flooding simulations. Consequently, the strength properties of CGSS and WGSS would have been higher than NSS. Furthermore, despite the moisture content increase in WGSS being just slightly smaller than CGSS for both rainfall and flooding simulations, WGSS was likely to have a greater CBR and a higher strength than CGSS due to the vulnerability of the subgrade materials in this moisture content range.

4.2 Sub-ballast and ballast fouling

Fines migration from subgrade to ballast layer can be induced by the accumulation of pore water pressure in the subgrade under repeated traffic loading. The migration of fine particles will lead to cohesive-type ballast fouling, which can significantly deteriorate the service performance of the sub-ballast and ballast. Further, as fouling develops beyond a certain level, the lateral resistance of the ballast will decrease significantly and additional deformation in the ballast layer will occur [30, 31]. Moisture and fouling ingredients may even interact with each other, leading to a remarkable decrease in stiffness and settlement behavior of the ballasted layer [32].

The fouling degree of the sub-ballast and top ballast layers were measured for the investigated models by sampling from the targeted locations. Fig. 14 presents the sampling locations in the sub-ballast and top ballast layers. The top ballast sample, denoted as TB-1, was obtained from the top ballast layer along the central line of the box. The sample was 20 cm in diameter and 30 cm in thickness. Four samples were collected from the sub-ballast layer for each test model. Two sub-ballast samples, labeled SB-1 and SB-2, were acquired along the central line. Both samples had a length of 60 cm, a width of 35 cm, and a thickness of 7.5 cm. SB-1 was the upper sample, and SB-2 was the lower one. The other two samples, which were labeled as SB-3 and SB-4 and had a diameter of 15 cm and a thickness of 15 cm, were obtained 50 cm away from the central line along the length direction of the model box.

The minimum particle size of the original sub-ballast and top ballast was 0.25 mm, and most soil particles in the subgrade section were finer than 0.25 mm. Therefore, the particles finer than 0.25 mm observed in the sub-ballast and top ballast after specified test phases were regarded as

fouling. The fouling degrees of sub-ballast and top ballast layers were evaluated using the equation:

$$\mu = \frac{m_1 - m_2}{m_2} \quad (1)$$

where m_1 was the mass of the oven-dried sample collected from the targeted location, m_2 was the mass of the oven-dried sample with particles finer than 0.25 mm excluded, and μ was the fouling degree of the sub-ballast or ballast.

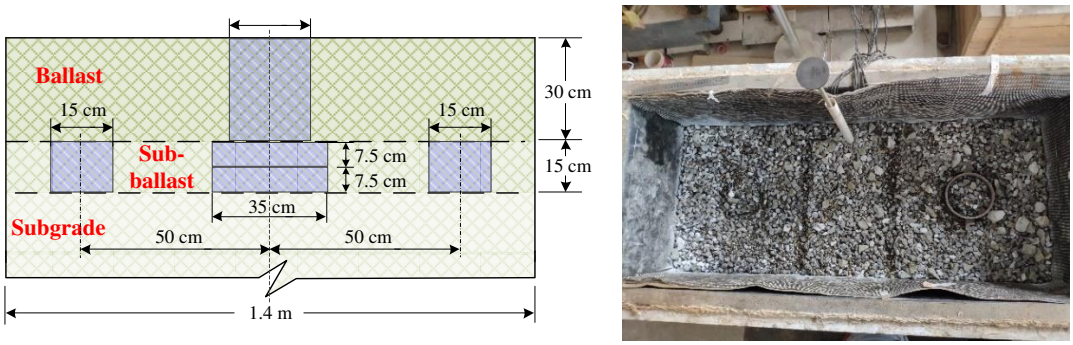

(a) (b)

Fig. 14 Sampling locations for fouling degree measurement: (a) sampling location diagram; (b) sampling location in the sub-ballast layer

Upon collection from the target location, the samples were dried and weighed to obtain their dry mass m_1. Then, the samples were placed in a 0.25 mm sieve and washed with water to remove the particles finer than 0.25 mm. After washing, the samples were dried and weighed again to obtain m_2. Then, the fouling degree was obtained via Eq. (1). Tables 3 and 4 quanitfy the fouling in the sub-ballast and ballast layers, respectively. Fig. 15 shows the comparison of fouling degrees in the sub-ballast and top ballast layers for a given test section. The lower portion of sub-ballast layer had the highest fouling degree for all of the test sections. Moreover, the ballast layer had the lowest fouling degree, ranging from 0.09% to 0.22% for the test sections. The upper portion of sub-ballast layer had the fouling degree that stayed at the intermediate level.

Since SB-1 and SB-2 were obtained from the upper and lower portions of sub-ballast layer along the central line, respectively, their average fouling degrees can be calculated to denote the fouling degree of the central portion of sub-ballast layer. The fouling degrees of the central portion were 2.27%, 1.28%, and 0.88% for NSS, CGSS, and WGSS, respectively. No remarkable difference was observed between the fouling degrees of the central portion and the portions 50 cm away from the central line for a given test model. Therefore, the average fouling of sub-ballast layer was

evaluated for the test models (Fig. 16). After the rainfall simulation, flooding simulation, and cyclic loading process, the fouling of sub-ballast layer in NSS reached 3.21%, which was more than twice that in CGSS and three times greater than that in WGSS. Further, the fouling of ballast layer of WGSS was also the lowest among the test sections.

Table 3 Fouling degree in sub-ballast layer

Model type	Sample No.	m_1/kg	m_2/kg	Fouling content/kg	Fouling degree/%	Average degree for SB-1 and SB-2/%	Average degree/%
NSS	SB-1	33.45	33.16	0.29	0.87	2.27	3.21
	SB-2	33.78	32.58	1.20	3.68		
	SB-3	7.79	7.48	0.31	4.20	4.20	
	SB-4	7.22	7.00	0.22	3.17	3.17	
CGSS	SB-1	32.26	31.90	0.36	1.13	1.28	1.50
	SB-2	32.74	32.28	0.46	1.43		
	SB-3	7.41	7.31	0.10	1.37	1.37	
	SB-4	5.19	5.10	0.09	1.86	1.86	
WGSS	SB-1	33.67	33.55	0.12	0.36	0.88	1.03
	SB-2	33.72	33.26	0.47	1.40		
	SB-3	6.67	6.60	0.07	1.06	1.06	
	SB-4	7.08	7.00	0.08	1.14	1.14	

Table 4 Fouling degree in ballast layer

Model type	m_1/kg	m_2/kg	Fouling content/kg	Fouling degree/%
NSS	28.40	28.36	0.04	0.14
CGSS	29.04	28.97	0.07	0.22
WGSS	27.87	27.85	0.03	0.09

The lower fouling in sub-ballast and top ballast layers of CGSS and WGSS was attributed to the separation and filtration function of the geotextile. However, the fouling in sub-ballast and ballast layers of WGSS were only 68.7% and 40.9% of that in CGSS, respectively. This was attributed to the capillary suction produced by the wicking geotextile on the accumulation of pore water pressure. Fouling migration upward into the sub-ballast and ballast layers was mainly induced by pore water pressures beneath the SS interface. Fig. 17 presents the pore water pressure at 10 cm below the interface during loading cycles in the three test phases. The pore water pressure of WGSS in Phase III was missed due to malfunction of the pressure sensor. Despite this, a sharp increase of pore water pressure was presented in NSS during the initial cyclic loading after flooding

simulation. In contrast, the pore water pressure in CGSS remained at a relatively low level. Consequently, the fouling in NSS was significantly higher than that in CGSS. For the same reason, the lower fouling degree in WGSS compared with CGSS was attributed to the capillary suction induced by wicking fibers in the geotextile and the lower pore water pressure in WGSS arising therefrom. Comparing the fouling in ballast and pore water pressure in the subgrade, it indicated that the wicking geotextile played a crucial part in preventing the development of pore water pressure and decreasing the fouling in the ballast layer under cyclic loading.

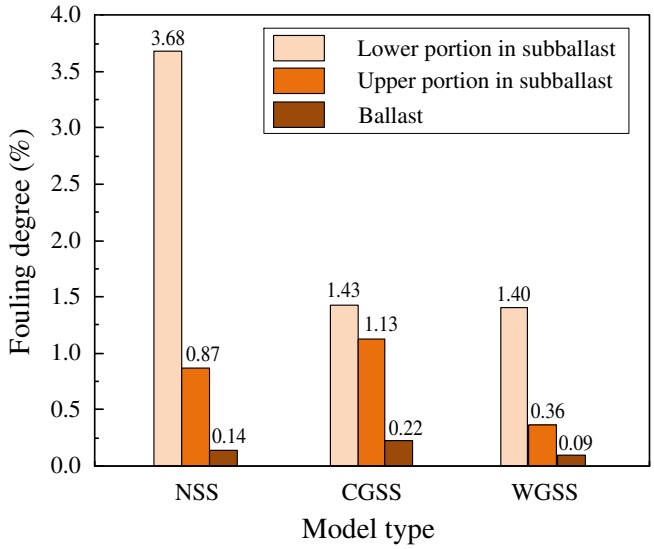

Fig. 15 Comparison of fouling in sub-ballast and ballast layers

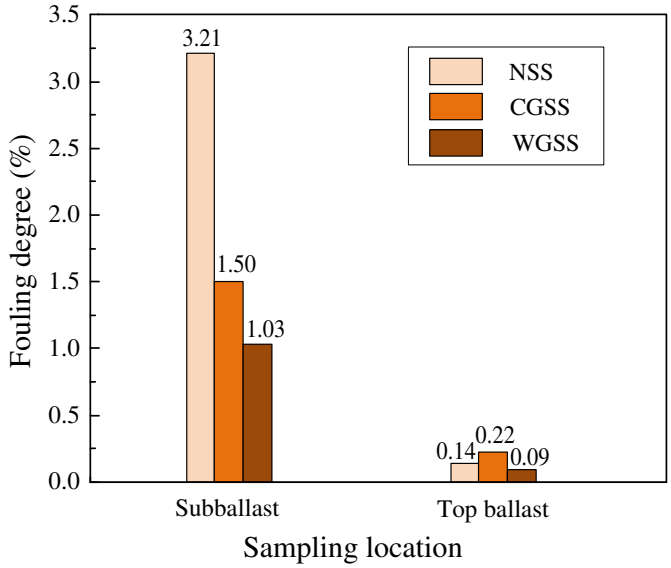

Fig. 16 Comparison of fouling degrees

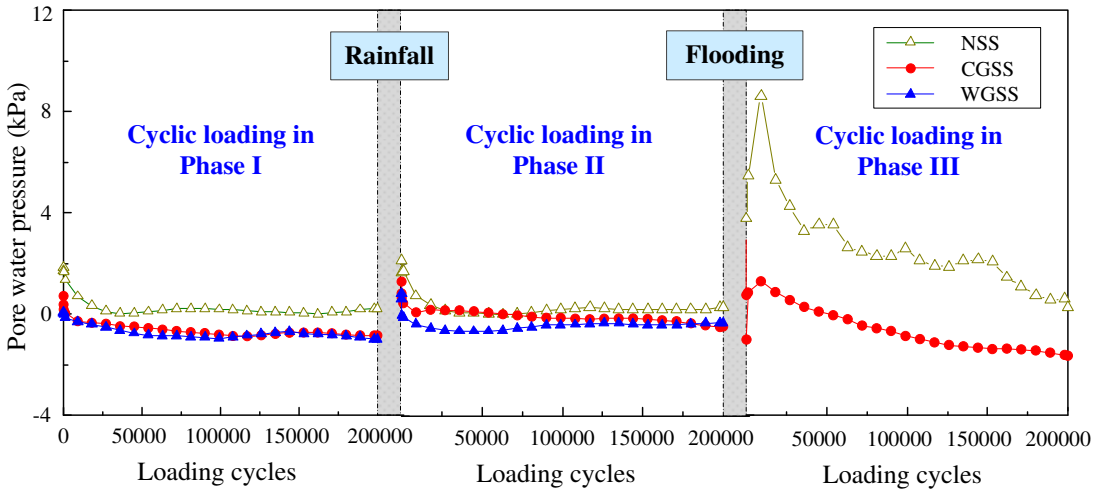

Fig. 17 Pore water pressure at 10 cm below the interface

4.3 Settlement

The settlements at ballast layer surface, TS interface, and SS interface were monitored by displacement transducers for the test sections (Fig. 18). For NSS, the settlements increased with loading cycles initially in Phase I, but they levelled off and gradually remained stable in the middle-to-later periods of Phase I. The surface settlement was the largest and reached 18.87 mm. The settlements of the TS and SS interfaces were 8.24 and 2.45 mm, respectively, after 200,000 loading cycles. Therefore, the deformations of the subgrade and sub-ballast were 2.45 and 5.79 mm, respectively. However, the deformation of the ballast layer was as high as 10.63 mm, indicating the surface settlement was dominated by the deformation of the ballast layer.

After rainfall, the settlements increased with loading cycles again, and similarly, they entered into a relatively steady state in limited loading cycles. The settlements at the top ballast surface, TS interface, and SS interface were 30.09, 10.31, and 5.85 mm, respectively, at the end of this loading phase. After flooding simulation, the settlements at different elevations increased continuously with loading cycles until the 200,000th loading cycle. The total settlement reached 84.18 mm, with deformation values of 40.03, 14.45, and 29.70 mm observed in the subgrade, sub-ballast, and top ballast, respectively. Perhaps more importantly, the settlements demonstrated a remarkable settlement increase after flooding and 200,000 loading cycles.

The settlement profile for CGSS differed from NSS. In the first cyclic loading stage, the settlements at different elevations were 20.78, 8.04, and 2.24 mm after 200,000 loading cycles, and these values remained close to those of NSS in Phase I. Again, the deformation in the ballast layer

was the main factor that induced surface settlement. After rainfall, the settlements gradually stabilized after a few initial cyclic loading cycles. The surface settlement rose to 30.67 mm, which was consistent with that of NSS. This result implied the conventional geotextile had minimal effect on reducing the settlement post-rainfall. Such an event can be attributed to the limited moisture content increase after the rainfall simulation for NSS and CGSS. However, the effect of conventional geotextiles was highlighted after flooding.

At the end of Phase III, the final surface settlement increased to 56.28 mm, which was 33.14% less than that of the NSS. Moreover, the deformations in the subgrade, sub-ballast, and ballast layers of CGSS were less than those of NSS, indicating the conventional geotextile played a vital role in separating the ballast layer from the subgrade and preventing the deformations of different functional layers from developing continuously. Additionally, the geotextile at the interface of the sub-ballast and subgrade provided lateral restraint and further produced a tensioned membrane effect that further decreased the vertical stress [33-35].

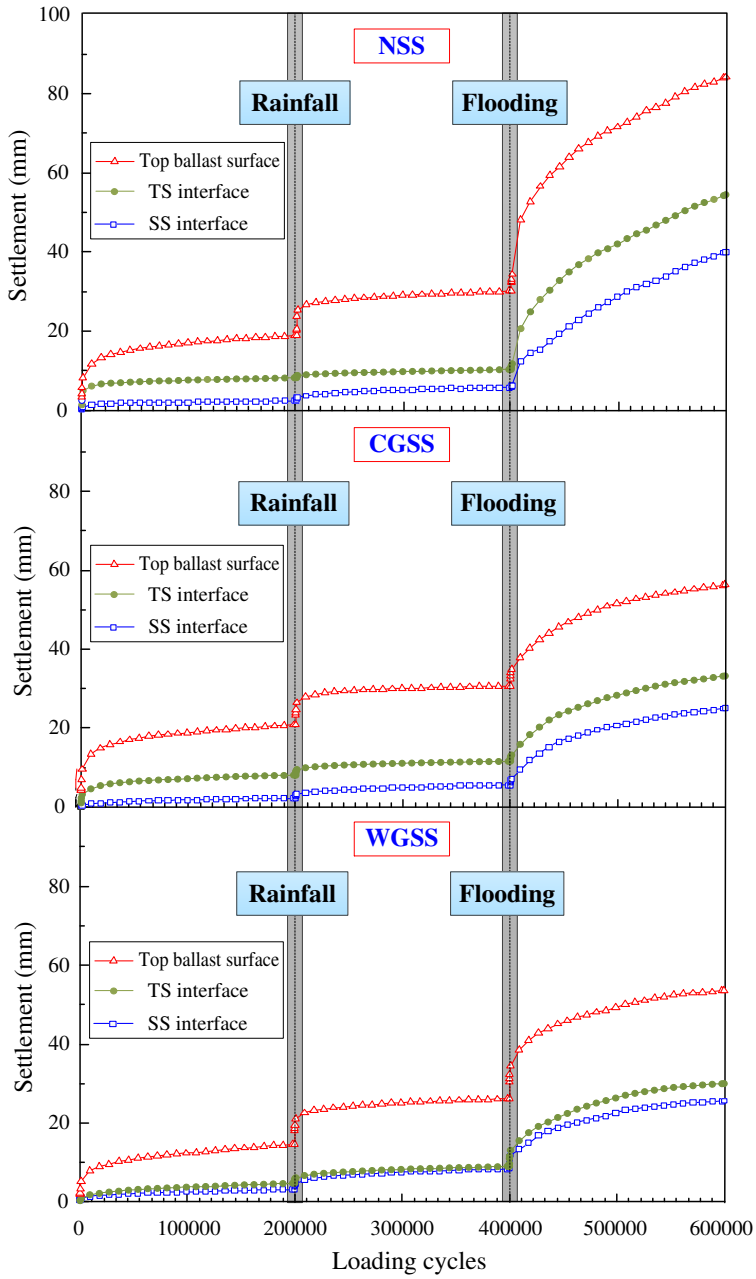

Fig. 18 Permanent settlement in the cyclic loading process for NSS, CGSS and WGSS.

The settlements at the different interfaces of WGSS demonstrated similar development features to those of CGSS. The final surface settlement after the three test phases was 53.60 mm, which was marginally smaller than CGSS (56.28 mm). This finding implies that the wicking geotextile had similar deformation resistance to the conventional one. Thus, although the capillary suction produced by wicking fiber in the wicking geotextile can help to decrease moisture content, inhibit pore water pressure generation, and prevent fines migration upward into the sub-ballast, the resultant deformation resistance was limited to 600,000 loading cycles compared with CGSS.

Despite a total of 600,000 loading cycles involved in this study, the finite loading cycles had certain limitations regarding the evaluation of long-term deformation behaviors of the test sections. As a result of these limited conditions, the influence of the fouling of the ballast on the long-term deformation behavior was not sufficiently reflected in the settlement test data after the three test phases. Meanwhile, the adverse effect of fouling ingredients on the lateral resistance of the ballast layer was difficult to simulate through a box-based model test. Thereby, the advantage of wicking geotextiles in resisting layer deformation and surface settlement was not highlighted in the model tests.

Despite this, the loading cycles needed to reach a certain amount of surface settlement (denoted as N_f) can be determined for NSS, CGSS and WGSS to investigate the effectiveness of conventional and wicking geotextiles in resisting long-term railway settlement. N_f corresponding to the surface settlements of 35 cm, 45 cm and 53 cm are determined for NSS, CGSS and WGSS in accordance with the permanent settlement data after flooding simulation. The surface settlement of 53 cm was chosen because the final surface settlement of WGSS after flooding simulation was only 53. 60 mm. The comparison of N_f for NSS, CGSS and WGSS is presented in Fig. 19.

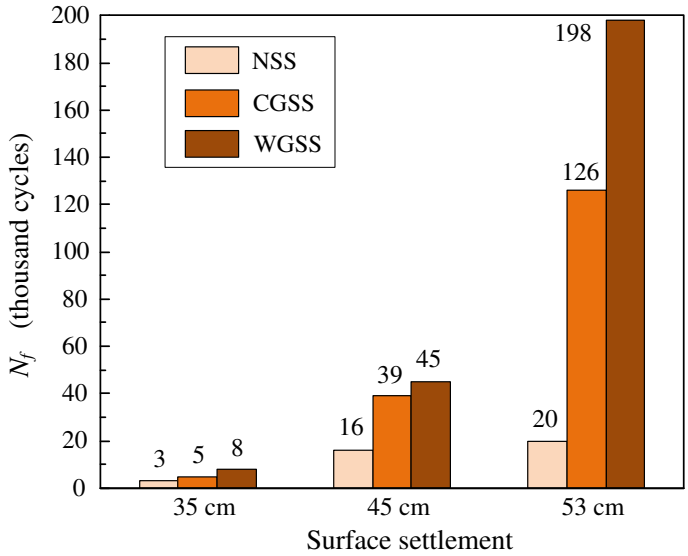

Fig. 19 Comparison of N_f

N_f of all the test sections increased with surface settlement. As settlement developed from 35 cm to 53 cm, N_f of NSS increased from 3 to 20. CGSS and WGSS had N_f that ranged from 5 to 126, and 8 to 198, respectively. The percentage increases of N_f for CGSS and WGSS were significantly larger

than that for NSS, while WGSS had the greatest increase in N_f amplitude. Furthermore, N_f of WGSS was 1.57 times that of CGSS at a settlement of 53 cm, indicating 1.57 times more loading cycles were needed for WGSS compared to CGSS to reach a settlement of 53 cm. Therefore, WGSS showed significant potential in preventing long-term deformation, and was expected to have a longer service life than CGSS.

As mentioned above, the wicking geotextile demonstrated a superior ability compared to the conventional one for inhibiting the migration of fines upwards, thus decreasing the fouling of ballast when subject to rainfall or flooding. Ballast fouling can lead to reduced strength and stiffness of the track structure [36, 37] and result in the loss of drainage capability. Therefore WGSS was likely to offer an increased ability to prevent deformation of the functional layers and preserve the track structure compared to CGSS. Thereby, an embankment stabilized using a wicking geotextile is more likely to have an excellent service performance compared with the same one stabilized using a the conventional geotextile.

5 Limitations

The capillary suction of the wicking geotextile was affected by air temperature and humidity. The variation in temperature and humidity may have influenced the wicking drainage efficiency during testing. The model test of WGSS was performed in Chengdu, Sichuan Province, in September, 2019. The mean daytime temperature during the test period was 25℃, and the mean night temperature was 18℃. The relative humidity varied from 80% to 84% during the whole test process. Thereby, the variations in temperature and humidity were minimal, and their influence on the wicking drainage efficiency was limited.

6 Conclusions

The ballast–subgrade performance in the presence of NSS, CGSS and WGSS were investigated in by performing large-scale laboratory tests. Each section underwent three test phases: stationary–loading (Phase I), rainfall–loading (Phase II) and flooding–loading phases (Phase III). The moisture content variation, fouling degree of ballast, and settlements at different elevations were monitored. Based on the test results, the conclusions were:

(1) Both conventional and wicking geotextiles can prevent rainfall water from infiltrating into

subgrade soils. The moisture content increases at 10 cm below the ballast–subgrade interface were only 6.4% and 6.0% for CGSS and WGSS, respectively, after rainfall simulation, which was lower than 8.7%, the moisture content increase of NSS.

(2) Wicking geotextile produces capillary suction, which significantly delays infiltration and helps to reduce the moisture content in subgrade soils. In testing, the moisture content increased at 25 cm below the interface initiated 10 h after the beginning of rainfall for WGSS. However, the incubation periods for moisture content increase were 3 h and 6 h for NSS and CGSS, respectively.

(3) Conventional and wicking geotextiles are capable of separation and filtration during rainfall and flooding simulation. This results in lower fouling: 1.50% and 1.03% of sub-ballast layers in CGSS and WGSS, respectively, compared to that of 3.21% in NSS. The lowest fouling degree observed in WGSS was attributed to the preventive capillary suction produced by the wicking geotextile during the accumulation of pore water pressure.

(4) The deformation resistance of wicking geotextile is similar to that of the conventional geotextile. However, the number of loading cycles needed to reach the same surface settlement is 1.57 times greater for WGSS than CGSS. Fines migration decreases the strength and stiffness of the track structure and lowers the lateral resistance of the ballast layers. Therefore WGSS are expected to exhibit lower long-term surface settlement compared with CGSS.

Acknowledgements

The study was sponsored by National Natural Science Foundation of China (grant numbers 51878560, 52008341, 52078427) and Natural Science Foundation of Sichuan Province, China (grant numbers 2022NSFSC0472 and 2022NSFSC1165). The non-wicking and wicking geotextiles adopted in this study were all provided by TenCate Geosynthetics.

References

[1] A.J. Choobbasti, M.A. Samakoosh, S.S. Kutanaei, Mechanical properties soil stabilized with nano calcium carbonate and reinforced with carpet waste fibers, Constr. Build. Mater. 211 (2019), 1094-1104.

[2] A. Bouazza, J.G. Zornberg, J.S. McCartney, H. Nahlawi, Significance of unsaturated behaviour of geotextiles in earthen structures, Australian Geomechanics. 41(3) (2006) 133-142.

[3] J. Han, Principles and Practice of Ground Improvement, John Wiley & Sons, 2015.

[4] A. Fakhrabadi, M. Ghadakpour, A.J. Choobbasti, S.S. Kutanaei, Influence of the Non-Woven Geotextile (NWG) on the engineering properties of clayey-sand treated with copper slag-based geopolymer, Constr. Build. Mater. 306 (2021), 124830.

[5] L. Zhang, X. Jiang, Z. Li, Z. Yang, G. Liu, Z. Dong, Y. Qiu, Influence of the attenuation of subgrade elastic modulus caused by precipitation on ballasted track structure, Constr. Build. Mater. 352 (2022),128971.

[6] K. Rajagopal, S. Chandramouli, A. Parayil, K. Iniyan, Studies on geosynthetic-reinforced road pavement structures, Int. J. Geotech. Eng. 8 (3) (2015) 287-298.

[7] D.G. Son, Y-H Byun, Shear strength characteristics of two-layer geotextile reinforced with flowable fill, Constr. Build. Mater. 367 (2023), 130207.

[8] J. Arivalagan, B. Indraratna, C. Rujikiatkamjorn, A. Warwick, Effectiveness of a Geocomposite-PVD system in preventing subgrade instability and fluidization under cyclic loading, Geotext. Geomembr. 50 (4) (2022) 607-617.

[9] C. Lin, J. Galinmoghadam, J. Han, J. Liu, X. Zhang, Quantifying and incorporating the benefits of wicking geotextile into pavement design, J. Transp. Eng. Part B: Pavements. 147 (2021), 04021044.

[10] J. Guo, J. Han, X. Zhang, Z.X. Li, Experimental evaluation of wicking geotextile-stabilized aggregate bases over subgrade under rainfall simulation and cyclic loading, Geotext. Geomembr. 49 (6) (2021) 1550-1564.

[11] J.G. Zornberg, Functions and applications of geosynthetics in roadways, Procedia Eng. 189 (2017) 298-306.

[12] Fatahi, B., Khabbaz, H., Liem Ho, H. Effects of geotextiles on drainage performance of ballasted rail tracks. Australian Geomechanics 46(4) (2011) 91-102.

[13] S.M. Luettich, J.P. Giroud, R.C. Bachus, Geotextile filter design guide, Geosynthetics in Filtration, Drainage and Erosion Control, 1992, 19-34.

[14] B. Kermani, M. Xiao, S.M. Stoffels, T. Qiu, Reduction of subgrade fines migration into subbase of flexible pavement using geotextile, Geotext. Geomembr. 46 (4) (2018) 377-383.

[15] C. Lin, X. Zhang, Comparisons of geotextile-water characteristic curves for wicking and non-

wicking geotextiles, Geo-Congress, 2020, 629-636.

[16] R.J. Bathurst, A.F. Ho, G. Siemens, A column apparatus for investigation of 1-D unsaturated-saturated response of sand-geotextile systems, Geotech. Test. J. 30 (6) (2007) 433-451.

[17] F. Wang, J. Han, X. Zhang, J. Guo, Laboratory tests to evaluate effectiveness of wicking geotextile in soil moisture reduction, Geotext. Geomembr. 45 (1) (2017) 8-13.

[18] J. Guo, J. Han, X. Zhang, Z. Li, Evaluation of moisture reduction in aggregate base by wicking geotextile using soil column tests, Geotext. Geomembr. 47 (3) (2019) 306-314.

[19] X. Zhang, W. Presler, L. Li, D. Jones, B. Odgers, Use of wicking fabric to help prevent frost boils in Alaskan pavements, J. Mater. Civil Eng. 26 (4) (2014) 728-740.

[20] J. Guo, F. Wang, X. Zhang, J. Han, Quantifying water removal rate of a wicking geotextile under controlled temperature and relative humidity, J. Mater. Civil Eng. (2016), 04016181.

[21] M. Bai, Z.B. Liu, S.J. Zhang, F. Liu, S.L. Lei, Drainage performance and capillary rise restraint effect of wicking geotextile, Journal of Central South University, 28 (10) (2021) 3260-3267.

[22] C. Lin, X. Zhang, J. Han, Comprehensive material characterizations of pavement structure installed with wicking fabrics, J. Mater. Civil Eng. 31 (2) (2019) 04018372.

[23] C. Lin, X. Zhang, J. Galinmoghadam, Y. Guo, Working mechanism of a new wicking geotextile in roadway applications: A numerical study, Geotext. Geomembr. 50(2) (2022) 323-336.

[24] C. Lin, W. Presler, X. Zhang, D. Jones, B. Odgers, Long-term performance of wicking fabric in Alaskan pavements, J. Perform. Constr. Fac. 31 (2) (2017) D4016005.

[25] I.E. Delgado, Use of geotextiles with enhanced lateral drainage in roads over expansive clays, Ph.D. dissertation, Dept. of Civil, Architectural, and Environmental Engineering, Univ. of Texas at Austin, 2015.

[26] M.T. Mchenry, M. Brown, J. Lopresti, J. Rose, R. Souleyrette, Use of matrix-based tactile surface sensors to assess fine-scale ballast-tie interface pressure distribution in railroad track, Transportation Research Record: Journal of the Transportation Research Board. 2476 (1) (2015) 23-31.

[27] C. Atalar, B.M. Das, E.C. Shin, D.H. Kim, Settlement of geogrid-reinforced railroad bed due to cyclic load, In: Proceedings of 15th International Conference on Soil Mechanics and Geotechnical Engineering, Istanbul, vol. 3, 2001, pp. 2045-2048.

[28] Railway Technical Research Institute, Design standards for railway structures and commentary (earth structures), Railway Bureau of the Ministry of Land, Infrastructure and Transport Government of Japan, Tokyo, 2000.

[29] H. Takemiya, X.C. Bian, Shinkansen high-speed train induced ground vibrations in view of viaduct-ground interaction, Soil Dyn. Earthq. Eng. 27 (6) (2007) 506-520.

[30] D.S. Budiono, T. McSweeney, M. Dhanasekar, N. Gurung, The effect of coal dust fouling on the cyclic behaviour of railtrack ballast, In Proceedings of the international conference on cyclic behaviour of soils and liquefaction phenomena, Bochum, 2004, 627–632.

[31] K. Giannakos, Loads on track, ballast fouling, and life cycle under dynamic loading in railways, J. Transp. Eng. 136 (12) (2010) 1075–1084.

[32] M. Esmaeili, P. Aela, A. Hosseini, Effect of moisture on performance of mixture of sand-fouled ballast and tire-derived aggregates under cyclic loading, J. Mater. Civil Eng. 31 (2) (2019) 04018377.

[33] J.P. Giroud, J. Han, Mechanisms governing the performance of unpaved roads incorporating geosynthetics, Geosynthetics. February/March, 2016, 23-33.

[34] X. Sun, J. Han, Mechanistic-empirical analysis of geogrid-stabilized layered system: Part I. Solution development, Geosynth. Int. 26 (3) (2019) 273-285.

[35] X. Sun, J. Han, J. Fei, J. Guo, W. Zhang, Geosynthetic-stabilized flexible pavements: solution derivation and mechanistic-empirical analysis, Geotext. Geomembranes. 48 (2020) 468-478.

[36] X. Chen, J. Zhang, Effect of clay invasion on shear behavior and dilatancy of unbound aggregate subbase, Transportation Geotechnics. 6 (2016) 16-25.

[37] B. Indraratna, N. Tennakoon, S. Nimbalkar, C. Rujikiatkamjorn, Behaviour of clay-fouled ballast under drained triaxial testing, Geotechnique. 63 (5) (2013) 410-419.